Chapter 4

Study of temperature-dependent crystallographic phase evolution in relaxor ferroelectric $(Ba_{0.85}Ca_{0.15})$ $(Sn_{0.11}Zr_{0.05}Ti_{0.84})O_3$ system

4.1 Introduction

Relaxors (or relaxor ferroelectrics) are the materials where there is no structural deformation at the macroscopic level with respect to the ideal cubic phase, but the electric dipoles are generated at local levels due to the presence of locally off-centered atoms in the global paraelectric cubic matrix [40, 146, 250]. Thus the relaxor behaviour is associated with the short-range ferroelectric ordering existing in the material, quite often quoted as polar nano-regions (PNRs) [40, 146, 250]. The polarization vectors of these PNRs are uncorrelated with each other, and thus, relaxors lack macroscopic spontaneous polarization [146]. In comparison to conventional ferroelectrics, relaxor ferroelectric materials offer

a number of advantages, such as low hysteresis loss, low hysteresis in the strain-field response, and minimum remnant polarization [251, 252]. Owing to their ability to exhibit outstanding electrostrictive strain, perovskite (ABO_3) based relaxor ferroelectrics are being consistently used in actuator applications [116, 253, 254, 255, 256]. In the previous chapter, we have analysed a $BaTiO_3$-based lead-free relaxor ferroelectric system $(Ba_{1-x}Ca_x)(Sn_{0.11}Zr_{0.05}Ti_{0.84})O_3$, where the temperature corresponding to dielectric maxima, *i.e.*, T_m lies in the vicinity of room temperature having high dielectric permittivity values [257]. In this chapter, we have performed temperature-dependent crystallographic phase transition studies for the composition $x = 0.15$.

4.2 Experimental procedure

The temperature-dependent X-ray diffraction measurements were carried out for the temperature range 100 K $\leq$ T $\leq$ 448 K during the heating cycle. The measurements were performed on a Cu-anode-based powder diffractometer operated in Bragg-Brentano geometry with a curved crystal monochromator [258]. The data was collected over the 2θ range 20^0 to 120^0 with a step size of 0.02, at a scan rate of 2^0 per minute. Further, all the temperature-dependent data have been subjected to Rietveld refinements performed via FULLPROF software [213]. In addition, to probe the local symmetry present in the global cubic phase, the temperature-dependent Raman measurements were also carried out using Horiba LabRAM HR at an excitation wavelength of 514.5 nm via Argon ion gas laser.

4.3 Result and discussion

4.3.1 Temperature-dependent X-ray diffraction analysis

The results obtained in the previous chapter by subjecting the synthesized ceramics $(Ba_{1-x}Ca_x)(Sn_{0.11}Zr_{0.05}Ti_{0.84})O_3$ to X-ray diffraction, temperature-dependent dielectric measurement, PE hysteresis loop measurement, and Raman spectroscopic analysis have demonstrated the presence of a relaxor ferroelectric behaviour for all the compositions. This relaxor behaviour results due to PNRs generated by local off-centered atoms driven correlated displacements corresponding to 'A' and 'B' sites. Thus in order to throw more light on the structural phase transition behaviour we have performed the temperature-dependent X-ray diffraction analysis for one of the important compositions, *i.e.,* $(Ba_{0.85}Ca_{0.15})(Sn_{0.11}Zr_{0.05}Ti_{0.84})O_3$ (BCSZT15). Fig. 4.1 shows the temperature-dependent evolution of 200, 220, and 222, X-ray diffraction peak profiles over the temperature range $100\ K \leq T \leq 448$ K. In the previous chapter, we have seen that the dielectric permittivity *vs.* temperature plot shows a single peak, and the macroscopic cubic to macroscopic rhombohedral phase transition is mediated via local rhombohedral phase for all the compositions. In view of the X-ray diffraction peak profile analysis, one may conclude a cubic phase if all the peaks exhibit a non-split character. On the other hand, a rhombohedral phase is characterized by the splitting of the peaks corresponding to $\{hh0\}$, $\{hhh\}$ reflections into two, while the non-split nature of the peak associated with the $\{h00\}$ reflections. From Fig. 4.1, one can clearly see a singlet nature of the peaks corresponding to 200, 220, and 222 reflections over the temperature range $248\ K \leq T \leq 448$ K, demonstrating a cubic-like phase. However, the presence of a hump can be seen in the peak profile, which has appeared due to $K\alpha_2$ radiation. With the further lowering of temperature below 248 K, an additional peak appears on the lower 2θ side corresponding to 222 reflection, indicating a transformation into a rhombohedral phase or a mixed phase with the coexisting cubic and rhombohedral
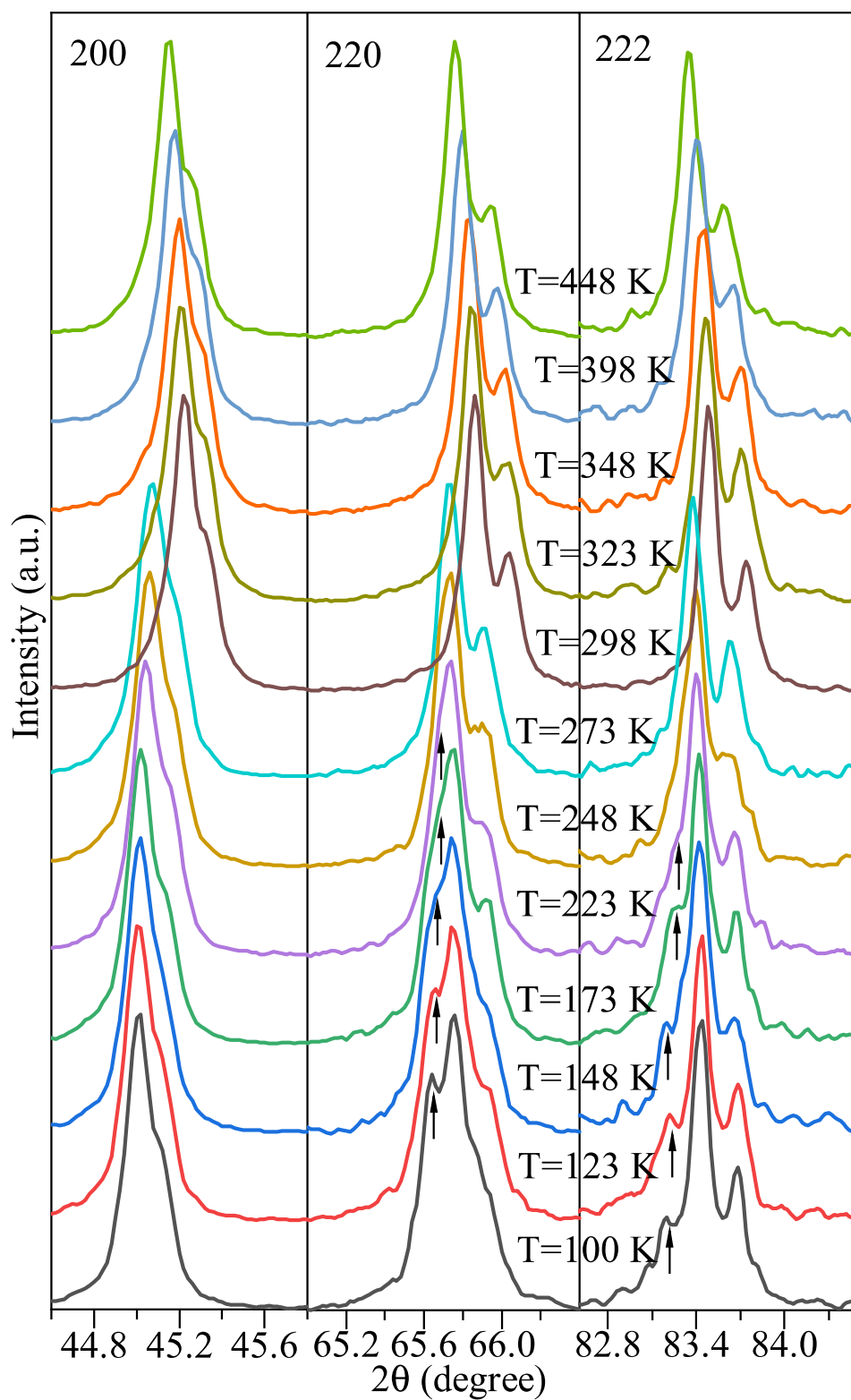
Fig. 4.1 Temperature-dependent evolution of the peak profile corresponding to 200, 220, and 222 reflections for BCSZT15.
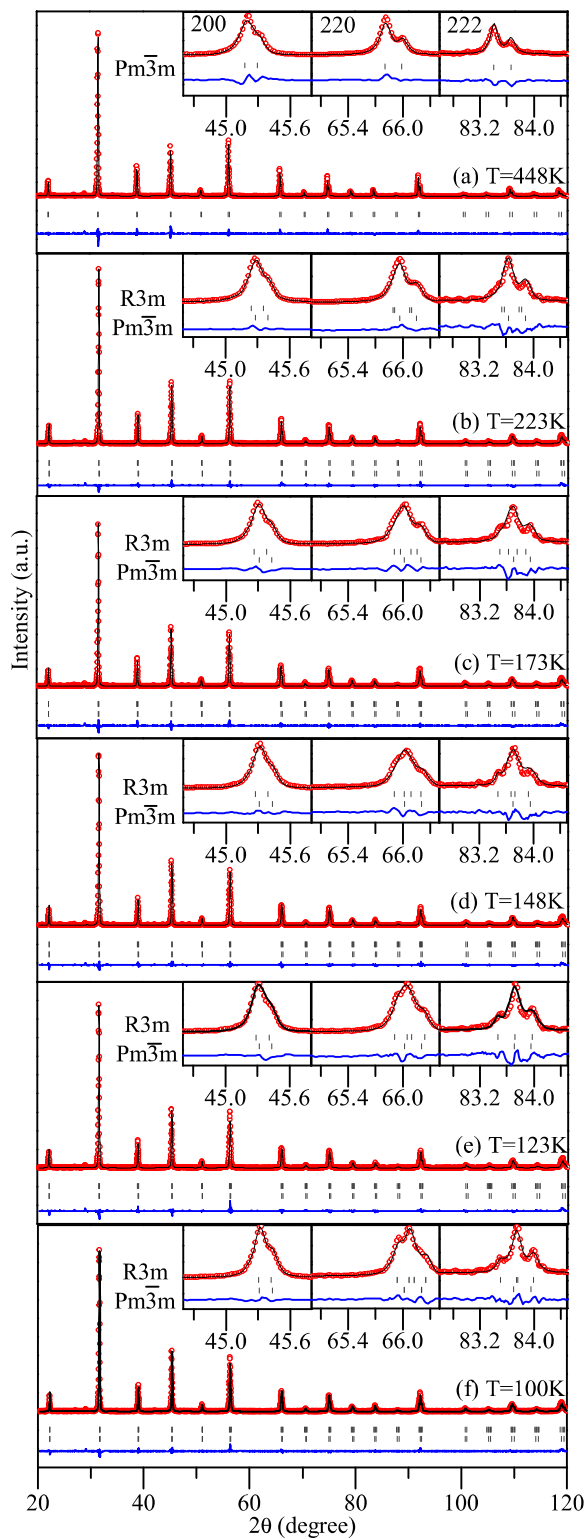
Fig. 4.2 Rietveld fitted temperature-dependent diffraction pattern of BCSZT15 at some selected temperatures.
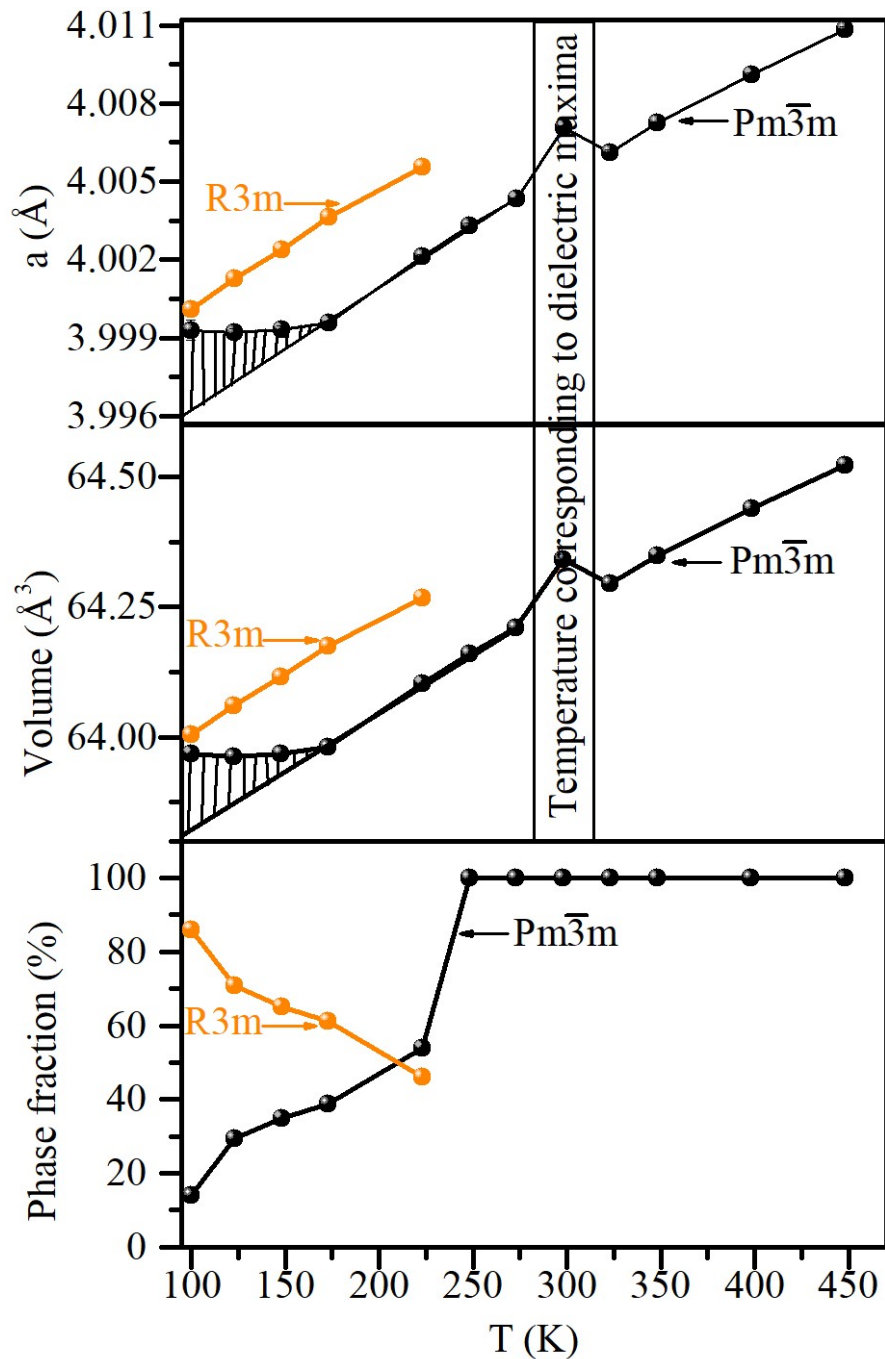
Fig. 4.3 Variation of lattice parameter, volume of the unit cell, and phase fractions with temperature for BCSZT15.

Table 4.1 Structural parameters and various agreement factors obtained from the Rietveld refinements of the temperature-dependent X-ray diffraction patterns for BCSZT15.

Atoms	WP	x	y	z	$U(\mathring{A}^2)$
			$T = 448$ K ($Pm\bar{3}m$)		
			Space group: $Pm\bar{3}m$		
Ba/Ca	1a	0.000	0.000	0.000	0.0064(3)
Ti/Sn/Zr	1b	0.500	0.500	0.500	0.0094(5)
O	3c	0.500	0.500	0.000	0.0156(14)
		$a = 4.01085(10)$ Å, $v = 64.522(3)$ Å^3			
		Agreement factors: $R_{wp} = 15.8$, $R_{exp} = 19.72$			
			$T = 223$ K ($Pm\bar{3}m$+$R3m$)		
			Space group: $Pm\bar{3}m$		
Ba/Ca	1a	0.000	0.000	0.000	0.0032(13)
Ti/Sn/Zr	1b	0.500	0.500	0.500	0.0090(17)
O	3c	0.500	0.500	0.000	0.001(3)
		$a = 4.00214(6)$ Å, $v = 64.103(2)$ Å^3			
		Phase fraction = 53.97%			
			Space group: $R3m$		
Ba/Ca	3a	0.000	0.000	0.000	0.0006(19)
Ti/Sn/Zr	3a	0.000	0.000	0.489(9)	-0.000(4)
O	9b	0.170(13)	0.340(13)	0.31(2)	0.000(9)
		$a = 5.6656(4)$ Å, $c = 6.9357(16)$ Å, $v = 192.80(5)$ Å^3			
		Phase fraction = 46.03%			
		Agreement factors: $R_{wp} = 16.4$, $R_{exp} = 21.60$			
			$T = 173$ K ($Pm\bar{3}m$+$R3m$)		
			Space group: $Pm\bar{3}m$		
Ba/Ca	1a	0.000	0.000	0.000	0.0030(15)
Ti/Sn/Zr	1b	0.500	0.500	0.500	0.007(3)
O	3c	0.500	0.500	0.000	0.001(5)
		$a = 3.99959(8)$ Å, $v = 63.980(2)$ Å^3			
		Phase fraction = 38.72%			
			Space group: $R3m$		
Ba/Ca	3a	0.000	0.000	0.000	0.0016(14)
Ti/Sn/Zr	3a	0.000	0.000	0.491(11)	0.001(5)
O	9b	0.17(2)	0.35(2)	0.33(2)	0.001(4)
		$a = 5.6594(4)$ Å, $c = 6.9408(8)$ Å, $v = 192.52(3)$ Å^3			
		Phase fraction = 61.28%			
		Agreement factors: $R_{wp} = 17.2$, $R_{exp} = 22.12$			

phases. In addition to the peak profile analysis, the Rietveld refinement of the entire diffraction pattern has been carried out for the quantitative phase analysis. However, prior

Table 4.2 Structural parameters and various agreement factors obtained from the Rietveld refinements of the temperature-dependent X-ray diffraction patterns for BCSZT15.

Atoms	WP	x	y	z	$U(\text{Å}^2)$
				T = 148 K ($Pm\bar{3}m$+$R3m$)	
			Space group: $Pm\bar{3}m$		
Ba/Ca	1a	0.000	0.000	0.000	0.0037(20)
Ti/Sn/Zr	1b	0.500	0.500	0.500	0.006(3)
O	3c	0.500	0.500	0.000	0.002(7)
		a = 3.99934(13) Å, v = 63.968(4) Å^3, Phase fraction = 34.89%			
			Space group: $R3m$		
Ba/Ca	3a	0.000	0.000	0.000	0.0013(12)
Ti/Sn/Zr	3a	0.000	0.000	0.497(11)	0.003(2)
O	9b	0.18(2)	0.36(2)	0.334(10)	0.001(11)
		a = 5.6561(3) Å, c = 6.9425(4) Å, v = 192.34(2) Å^3, Phase fraction = 65.11%			
		Agreement factors: R_{wp} = 17.7, R_{exp} = 22.35			
				T = 123 K ($Pm\bar{3}m$+$R3m$)	
			Space group: $Pm\bar{3}m$		
Ba/Ca	1a	0.000	0.000	0.000	0.0044(20)
Ti/Sn/Zr	1b	0.500	0.500	0.500	0.008(4)
O	3c	0.500	0.500	0.000	0.003(6)
		a = 3.99920(17) Å, v = 63.962(5) Å^3, Phase fraction = 29.28%			
			Space group: $R3m$		
Ba/Ca	3a	0.000	0.000	0.000	0.0028(14)
Ti/Sn/Zr	3a	0.000	0.000	0.492(6)	0.003(4)
O	9b	0.179(19)	0.358(19)	0.332(8)	0.011(7)
		a = 5.6534(3) Å, c = 6.9432(4) Å, v = 192.18(2) Å^3, Phase fraction = 70.72%			
		Agreement factors: R_{wp} = 18.1, R_{exp} = 22.60			
				T = 100 K ($Pm\bar{3}m$+$R3m$)	
			Space group: $Pm\bar{3}m$		
Ba/Ca	1a	0.000	0.000	0.000	0.002(5)
Ti/Sn/Zr	1b	0.500	0.500	0.500	0.014(10)
O	3c	0.500	0.500	0.000	0.002(17)
		a = 3.99933(39) Å, v = 63.968(11) Å^3, Phase fraction = 13.98%			
			Space group: $R3m$		
Ba/Ca	3a	0.000	0.000	0.000	0.0010(12)
Ti/Sn/Zr	3a	0.000	0.000	0.493(5)	0.001(2)
O	9b	0.177(16)	0.354(16)	0.333(7)	0.000(6)
		a = 5.6521(1) Å, c = 6.9403(3) Å, v = 192.01(1) Å^3, Phase fraction = 86.02%			
		Agreement factors: R_{wp} = 17.5, R_{exp} = 22.74			

to the Rietveld refinements, the lattice parameters were fixed by performing the Le-Bail refinement of the entire diffraction pattern; thereafter, the diffraction data were subjected to the Rietveld refinements. The refined parameters include 2θ-zero, background fitted by linear interpolation between a set background points with refinable heights, lattice parameter, FWHM parameters, pseudo-Voigt profile shape parameters, atomic positional coordinates, and the thermal displacement parameters. The Rietveld refinements performed with the single cubic phase having ($Pm\overline{3}m$) space group were successful in taking into account all the features observed in the diffraction pattern for the temperature range 248 K $\leq$ T $\leq$ 448 K. Thus, our Rietveld analysis confirmed a single cubic ($Pm\overline{3}m$) phase for the temperature range 248 K $\leq$ T $\leq$ 448 K. The temperature-dependent evolution of the Rietveld fitted diffraction patterns can be seen in Fig. 4.2. However, for the temperatures below 248 K, the data could not be fitted via a single cubic ($Pm\overline{3}m$) phase due to the appearance of an additional peak towards lower 2θ side corresponding to 222 reflection. Therefore, due to splitting observed in the peaks corresponding to 222 reflections, we have tried the refinements with the single rhombohedral ($R3m$) phase, where we could not find a satisfactory fit. Therefore, we tried the structural refinements below 248 K using a two-phase ($Pm\overline{3}m$+$R3m$) model, which gives a satisfactory fit between the observed and simulated diffraction patterns, as shown in Fig. 4.2. Thus, for the temperature range 100 K $\leq$ T $\leq$ 223 K, our analysis reveals the coexistence of the disordered cubic ($Pm\overline{3}m$) phase with the ordered rhombohedral ($R3m$) phase, where the local random displacements present at the high temperatures become completely ordered consistent with the constraints imposed by the rhombohedral symmetry.

The lattice parameters (a), the volume of the unit cell (v), and the fractions of the phases obtained from the Rietveld refinements of some of the temperature-dependent X-ray diffraction data are summarized in Tables 4.1 and 4.2. Fig. 4.3 shows the variations in these quantities as a function of temperature. As far as the temperature decreases, the

lattice parameter, and thus, the unit cell volume, decreases for the single cubic phase observed till T = 248 K (see Fig. 4.3). On further lowering the temperature, a completely ordered rhombohedral ($R3m$) phase appears in addition with the high-temperature cubic phase. The lattice parameter and unit cell volume corresponding to the $R3m$ phase show a decreasing trend till the lowest temperature. However, the lattice parameter and the unit cell volume corresponding to the cubic ($Pm\overline{3}m$) phase decrease till 173 K, but on further lowering the temperature, it becomes nearly independent of temperature, indicating the presence of electrostriction-like behaviour in the material (see Fig. 4.3). In addition, an anomaly in the lattice parameter and unit cell volume can be seen around 300 K, which is due to the appearance of temperature corresponding to the dielectric maxima in the vicinity of room temperature, as shown in chapter 3.

Previous studies have shown that the electrostrictive coefficient of a material is strongly influenced by the order-disorder behaviour of the 'B' site cation [251, 252, 259]. Additionally, as the ordering nature associated with the cation at the 'B' site progresses from a disordered state to a partially ordered one and finally into a completely ordered state, the electrostrictive coefficient exhibits an increasing nature. The electrostrictive effect describes the nonlinear (second-order or quadratic) dependence of the strain on the applied electric field [260]. The electrostriction is a four-rank tensor and can be observed in all crystal symmetries. It is a basic electromechanical phenomenon observed in all insulators or dielectrics and refers to the deformation effect, which describes the polarization (P_i)/electric field (E_i)-induced strain expressed as [251, 259]

$$S_{ij} = Q_{ijkl}P_kP_l \tag{4.1}$$

$$S_{ij} = M_{ijkl}E_kE_l \tag{4.2}$$

where Q_{ijkl} and M_{ijkl} are electrostrictive coefficients. In the disordered phase, the smaller 'B' site cation finds a significant amount of accessible space within the octahedra because the larger 'B' ions prop open the lattice framework. On the other hand, the octahedral space available for the rattling of the 'B' site cation gets reduced in the ordered state because the nearby oxygen atoms form a dense packing around the smaller 'B' site cation. Therefore if the disordered and ordered state both are subjected to an external electric field, then the 'B' site cation present in the disordered state will easily move within the octahedra without causing any distortion in the octahedral cage. Thus the application of an electric field in the disordered phase will give rise to a large polarization and lower strain, resulting in a small electrostrictive coefficient. However, in the ordered phase, the movement of the 'B' site cation is accompanied by distortion in the octahedra and thus gives rise to a large electrostrictive coefficient [251, 252, 259]. In BCSZT15 ceramic, we see that as a function of temperature, the phase is getting transformed from a completely disordered to partially disordered and finally into an ordered rhombohedral phase. Thus one can expect a good electrostrictive coefficient by the BCSZT15 ceramics, a glimpse of which has been reflected in the temperature-dependent evolution of lattice parameters and unit cell volume.

4.3.2   Temperature-dependent Raman spectroscopic studies

In order to investigate the persistence of short-range atomic ordering in the cubic phase, as demonstrated by temperature-dependent dielectric and PE hysteresis loop studies (see chapter 3), we have carried out temperature-dependent Raman spectroscopic studies. The basic matrix of BCSZT15 is average cubic with $Pm\overline{3}m$ space group. The cubic phase has five atoms per unit cell which gives rise to 12 optical and 3 acoustic modes of vibrations. In the cubic phase, the phonon mode belonging to zone center corresponds to $3T_{1u}+T_{2u}$ irreducible representations, with both T_{1u} and T_{2u} modes being triply degenerate in nature [239, 261]. Further, each of these modes exhibits an odd symmetry with respect to inversion
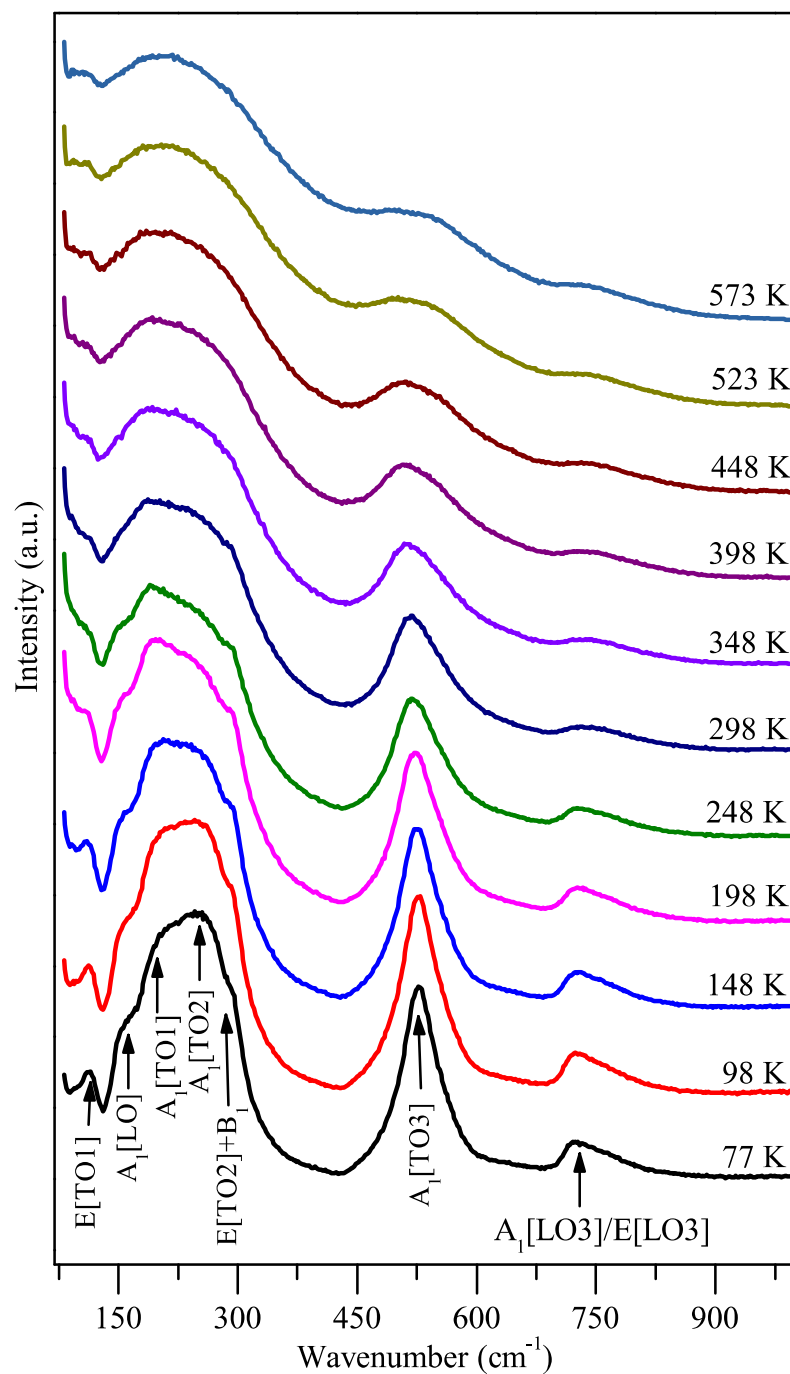
Fig. 4.4 Temperature-dependent Raman spectra of BCSZT15.

center, and hence no Raman activity is exhibited by these modes [238]. Since the temperature-dependent dielectric and X-ray diffraction studies have shown the presence of only cubic to rhombohedral phase transition for BCSZT15, the group theoretical analysis shows that at the cubic to the rhombohedral phase transition, the T_{1u} phonon mode splits into A_1 and E modes while T_{2u} mode splits into A_2 and E modes with the A_1 and E modes being Raman active while A_2 mode is Raman inactive [239, 257]. The temperature-dependent Raman spectra of BCSZT15 ceramic is shown in Fig. 4.4. At the lowest temperature, *i.e.,* 77 K, the Raman spectra exhibits seven modes, *viz.,* E[TO1], A_1[LO], A_1[TO1], A_1[TO2], E[TO2]+B_1, A_1[TO3], A_1[LO3]/E[LO3]. In addition to these modes, an anti-resonant dip around 130 cm^{-1} can be seen, which results due to coupling between A_1[TO1] and A_1[TO2] phonon modes [262, 263]. In the previous studies, it has been widely demonstrated that the E[TO1] and A_1[LO] modes appear only in the rhombohedral phase [264]. The lowest temperature Raman spectra matches well with that of the rhombohedral phase of $BaTiO_3$, and further, the presence of all these modes corresponding to the rhombohedral phase can be seen till 223 K. However, the X-ray diffraction data could not be fitted with the single rhombohedral (*R3m*) phase over the temperature range 100 K $\leq$ T $\leq$ 223 K, and the X-ray diffraction analysis has revealed the *Pm$\overline{3}$m+R3m* phase coexistence for the temperature range 100 K $\leq$ T $\leq$ 223 K. On the other hand, above the temperature 223 K, the X-ray diffraction analysis shows a single cubic phase with *Pm$\overline{3}$m* space group, but the Raman spectra still show the characteristic E[TO1] mode of the rhombohedral phase, which demonstrates that the local rhombohedral clusters are persisting even in the cubic phase, consistent with the relaxor ferroelectric behaviour shown by BCSZT15 ceramics in temperature-dependent dielectric studies discussed in chapter 3.

4.4   Conclusion

In conclusion, a detailed temperature-dependent structural phase transition studies have been performed for BCSZT15, demonstrating the existence of a single cubic ($Pm\overline{3}m$) phase for 248 K $\leq$ T $\leq$ 448 K, while the coexistence of cubic and rhombohedral ($Pm\overline{3}m+R3m$) phases for 100 K $\leq$ T $\leq$ 223 K. Further, the investigation of the lattice parameters and unit cell volume calculated via Rietveld refinements of temperature-dependent X-ray diffraction data have revealed the presence of an electrostrictive like behaviour for BCSZT15.

In the next chapter, we have analysed the role of long-range ordered inter-ferroelectric phase boundaries (driven by freezing of zone center phonon modes associated with the cubic phase) in tuning the ferroelectric properties of an eco-friendly functional material.